STM JOURNALS

International Journal of
Electro-Mechanics and
Material Behavior

Volume 4, Issue 1, 2026
January–June
DOI Journal: 10.37591/IJEMB

https://journals.stmjournals.com/ijemb

Review IJEMB

Ag_2S–Ag Nanocomposites: A Bottom-Up Approach to Enhance Thermoelectric Power Factor at Near Room Temperature

Anish Kumar[1,*]

Abstract

The intrinsic ductility, low toxicity, and naturally occurring abundance of silver sulphide (Ag_2S) have made it a potential thermoelectric material in recent years. However, high electrical resistance severely limits its practical application. Here, we present a thorough analysis of how metallic Ag nanoinclusions affect the structural, electrical, and thermoelectric characteristics of Ag_2S nanocomposites made using a simple bottom-up polyol approach. $(Ag_2S)_{1-x}Ag_x$ nanocomposites with an Ag content ranging from 0 to 26.1% were produced by controlling the inclusion of Ag nanoparticles by adjusting the proportion of sulphur precursor. X-ray diffraction with Rietveld refinement, FESEM-EDX, and X-ray photoelectron spectroscopy are used in structural and phase investigations to confirm the coexistence of monoclinic α-Ag_2S and face-centered cubic Ag phases with uniform interfacial distribution.A semiconductor-to-metal transition controlled by percolative charge transport through Ag-rich grain boundaries is observed together with a consistent decrease in resistivity with increasing Ag concentration, according to electrical transport measurements. Interestingly, for modest amounts of Ag nanoinclusion, improved Seebeck coefficients close to room temperature are seen, which is explained by low-energy charge carrier filtering at semiconductor–metal contacts. The composite comprising approximately 20.1% Ag achieves a maximum figure of merit ZT = 0.0029 at 325 K and an optimised thermoelectric power factor of 19.53 $\mu W \cdot m^{-1} \cdot K^{-2}$. These findings show that Ag nanoinclusion offers a practical means to separate electrical conductivity and Seebeck coefficient in Ag_2S, creating a feasible route toward mechanically sound, ecologically safe thermoelectric materials that function close to ambient temperature.

Keywords: Ag_2S nanocomposites, Ag nano inclusions, thermoelectric materials, Seebeck coefficient, carrier filtering, electrical transport, power factor.

INTRODUCTION

For our long-term sustainability, energy production from alternative sources that produce less waste heat, hazardous gases, or noise is crucial. Researchers are very interested in thermoelectric (TE) devices because of their high power consumption requirements. TE devices have a long lifespan and require little maintenance. They also quietly transform waste heat into power without creating any hazardous byproducts. Highly efficient TE materials are required in order to meet the objective of their compatibility with traditional energy sources. The dimensionless figure of merit $ZT = \alpha 2T/(\rho\kappa)$ determines the performance of thermoelectric devices, where ρ, κ, and T stand for

***Author for Correspondence**
Anish Kumar
E-mail: roniesomadder@gmail.com

[1]Assistant Professor, Department of Mechanical engineering, BIT, Sindri, Jharkhand, India

Received Date: February 24, 2026
Accepted Date: March 07, 2026
Published Date: March 25, 2026

Citation: Anish Kumar. Ag_2S–Ag Nanocomposites: A Bottom-Up Approach to Enhance Thermoelectric Power Factor at Near Room Temperature. International Journal of Electro-Mechanics and Material Behavior. 2026; 4(1): 40–55p.

electrical resistivity, total thermal conductivity, and absolute temperature, respectively [1,2]. Building solid materials with high α and σ (1/ρ) yet low κ is the primary problem. The best emerging materials for this are semiconductors, where κ can be reduced in a number of methods, including by introducing point defects, nanostructuring, and choosing highly anisotropic layered materials with heavy constituent elements in large unit cells. The reduction of grain size to the nanoscale [1,3,4], the introduction of nanocrystals into nanomaterial hosts [5-8], and the introduction of nanoparticles in bulk hosts [2,9,10] are the three ways that nano structuring is recognised as a potential method.

The creation of nanocomposites by introducing nanocrystals in nanomaterials/bulk host is a unique strategy for simultaneously reducing κ through combined grain boundary scattering of heat carriers and enhancing power factor (α2/ρ) induced by low energy charge carrier filtering [2,5-11]. Nanostructuring alone can achieve a good ZT value (~300 K) [1,3,4] The synthesis of Bi2Te2.7Se0.3/SnS2 nanocomposites using the polyol method was demonstrated by Li et al. [8]. They reported an enhanced ZT ~ 0.93 at 450 K for this nanocomposite with 1.47 vol% of SnS2, which was 2.3 times higher than that of pristine Bi2Te2.7Se0.3. Mehta et al. [4] showed a readily scalable bottom-up approach to create bulk TE nanomaterials of both n- and p-type pnictogen chalcogenides with ZT > 1 at 300 K. They explained the improvement by pointing to the exact control of SnS2 layer thickness, which drives the low energy charge carrier filtering effect and phonon scattering from the atomically thin interface of Bi2Te2.7Se0.3/SnS2 nanocomposites [8].

In p-type PbTe, Endo axially nanostructured with 4 mol% SrTe, and mesostructured with powder processing and spark plasma sintering, Biswas et al. [2] obtained a ZT value of 2.2 at 915 K. The amplification was ascribed to mesoscale grain boundaries, nanoscale Endo axial precipitates, and point defects scattering phonons on several scales.

Unfortunately, in addition to rare and hazardous materials (Pb, Te, Se, Bi, Sb, etc.), the most promising TE devices now on the market are hard and inflexible with very little ductility or brittleness. Additionally, they can readily break or crack due to careless handling errors, which can result in device failure and ultimately cause environmental issues because of the poisonous compounds in them [12].

This tends to restrict their use in some contexts, such as automobiles. It is a direct, narrow band-gap (~1.1 eV) layered semiconductor with relatively large absorption coefficients (~ 106 cm-1) [13-16], high chemical stability, natural abundance, and negligible toxicity [17]. It is gaining a lot of attention because of its potential uses in resistance switches, nonvolatile memory devices, photocatalysts, solar cells, and thermoelectric devices [18], as well as its good antibacterial qualities [19], photocatalysts, and solar cells [20-22]. Ag2S has the potential to be a TE material since its electronegativity difference (Δχ) among its constituent elements is 0.65, which is very near to the value of < 0.5 needed for a greater TE power factor (increased carrier mobility) [23]. For single phase Ag2S bulk, this value of α is greatly increased to around α400K = -625 μV/K [13]. Its high electrical resistance (>106 Ω) has drawn little attention despite its relatively high α and low κ [13,21,22]. By adjusting the atomic ratio of Ag:S and decreasing ρ through crystallite size variation, they propose that the thermoelectric performance of Ag2S can be enhanced at low temperatures [13,21,22].

EXPERIMENTAL SECTION

Method

We simply decreased the amount of thiourea in the aforementioned synthesis processes to insert Ag NPs into Ag2S nanomaterials, resulting in the creation of Ag2S-Ag nanocomposites. While maintaining the same reaction settings and procedures, samples containing varying amounts of thiourea, such as 7.5, 3, 2.85, 2.75, 2.7, 2.65, 2.6, and 2.55 mmol, were produced with a fixed 6 mmol of Ag-source. The sequence of (Ag2S)1-xAgx nanocomposites with predicted x = 0, 0, 9.52, 15.38, 18.18, 20.09, 23.53, and 21.09 percent are finally produced as a result. ASA0, ASA1, ASA2, ASA3, ASA4, ASA5, ASA6, and ASA7 are their respective codes.

RESULTS AND DISCUSSION

X-ray Diffraction and Energy Dispersive Analysis of X-ray Studies

The final composite's electrical and thermal conductivity as well as its thermoelectric characteristics will be determined by controlling the phase fractions of metallic Ag NPs and insulating Ag2S under the reaction conditions during their production. This has been made possible by methodically altering the amount of thiourea (S-source) to create a range of samples with various Ag:S ratios (section 1.2). Phase purity and crystallinity are initially determined by powder X-ray diffraction (XRD) of the resultant products (Figure 1).

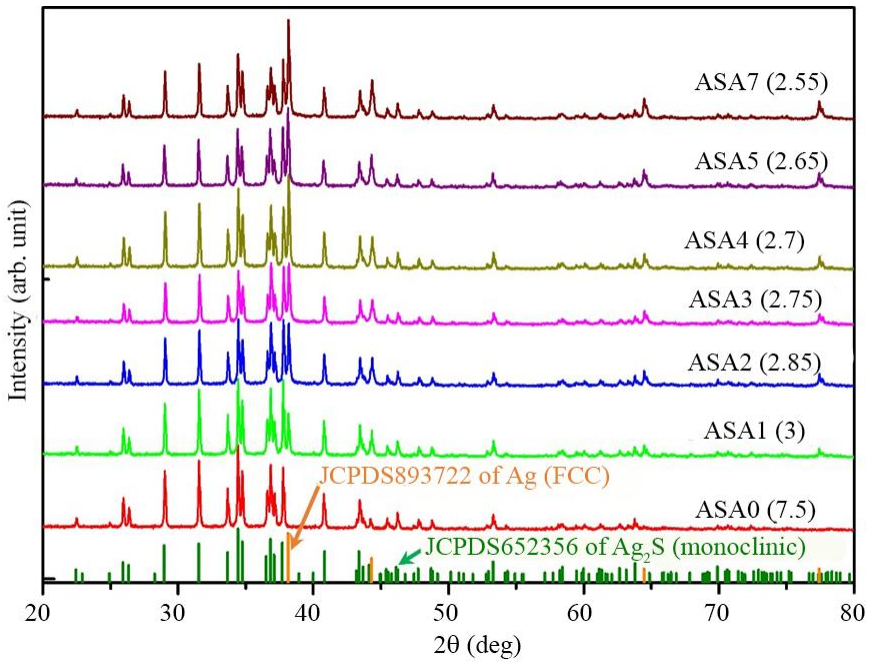

Figure 1. Ag2S-Ag powder XRD spectra of Ag2S-Ag nanocomposites made with a fixed Ag-source and altering the amount of thiourea from 2.55 to 7.5 mmol (in brackets). Standard reference cards bearing the JCPDS number are placed at the bottom of the spectrum.

Table 1. For both monoclinic (M) Ag2S and FCC Ag phases, the parameters derived via Rietveld refinement of all samples made with various amounts of thiourea (TU) with fixed AgNO3 are shown; the errors are indicated in parenthesis.

Parameters ↓ (AgNO3:TU) →	**ASA0** (6:7.5)	**ASA1** (6:3)	**ASA2** (6:2.85)	**ASA3** (6:2.75)	**ASA4** (6:2.7)	**ASA5** (6:2.65)	**ASA6** (6:2.6)	**ASA7** (6:2.55)
a(Å) M FCC	4.227(1)	4.226(1) 4.087(1)	4.227(1) 4.087(1)	4.227(1) 4.087(1)	4.228(1) 4.087(1)	4.226(1) 4.086(1)	4.226(1) 4.086(1)	4.228(1) 4.087(1)
b (Å)	1.927(1)	1.926(1)	1.928(1)	1.927(1)	1.928(1)	1.926(1)	1.927(1)	1.928(1)
c (Å)	9.533(1)	9.534(1)	9.534(1)	9.533(1)	9.534(1)	9.531(1)	9.532(1)	9.535(1)
V(Å3) M FCC	227.061	227.028 68.254	227.14 68.276	227.037 68.239	227.10 68.25	221.941 68.211	227.004 68.221	227.165 68.266
ρv (g/cm3) M FCC	7.230	07.270 10.284	07.274 10.278	07.272 10.290	07.261 10.284	07.297 10.290	07.251 10.288	07.240 10.283
β (o)	125.576	125.549	125.559	125.566	125.578	125.570	125.565	125.567
f0 (%) M [nominal] FCC [nominal]	100 [100] 0 [0]	93.45 [100] 01.55 [0]	88.85 [90.48] 11.15 [9.52]	87.69 [84.62] 12.31 [15.38]	85.77 [84.82] 14.23 [18.18]	85.19 [79.11] 14.81 [20.09]	84.65 [71.47] 15.35 [23.53]	80.99 [73.91] 19.01 [21.09]
ρv measured (g/cm3)	7.019	7.121	7.434	7.478	7.507	7.547	7.571	7.592

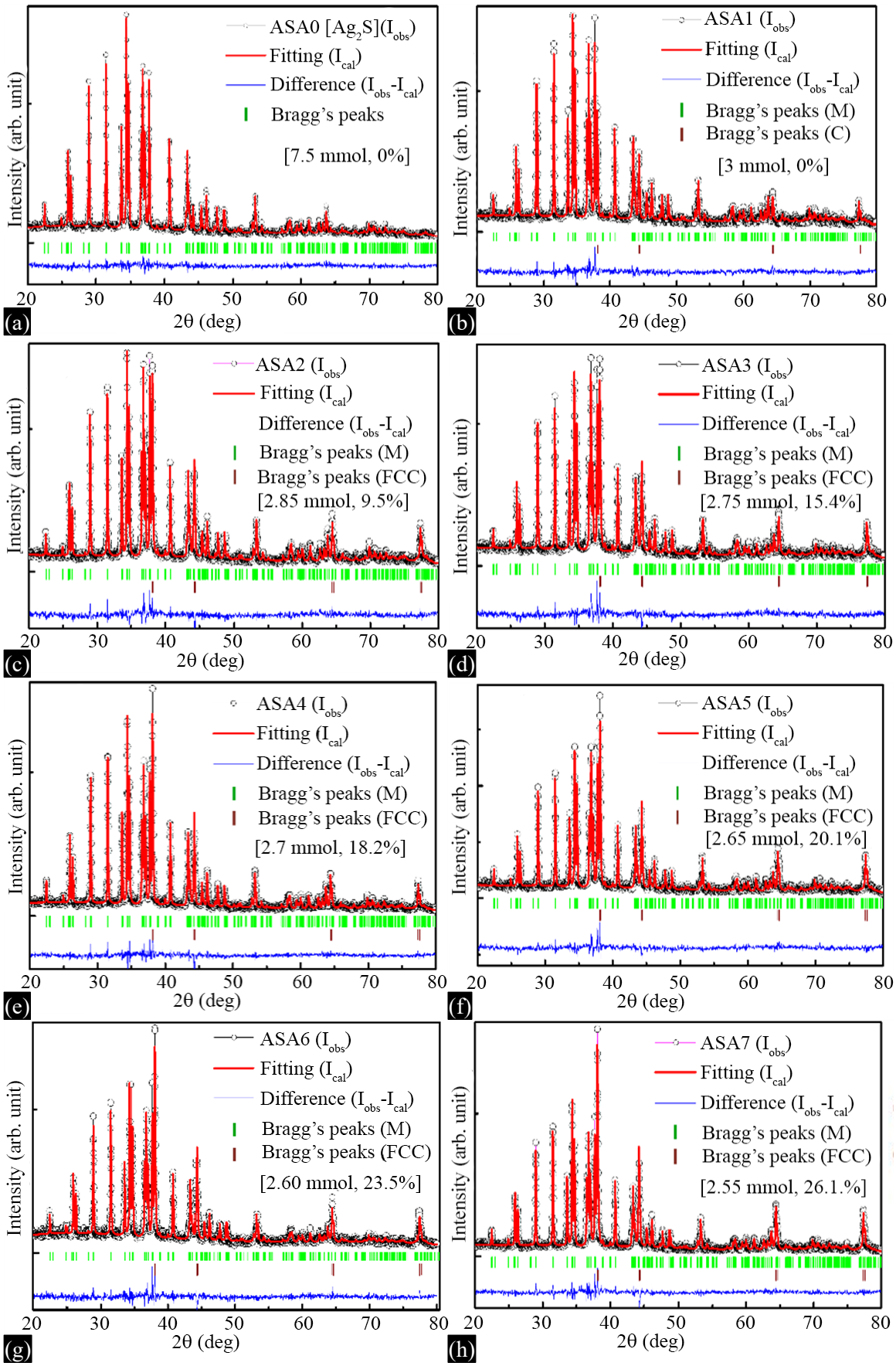

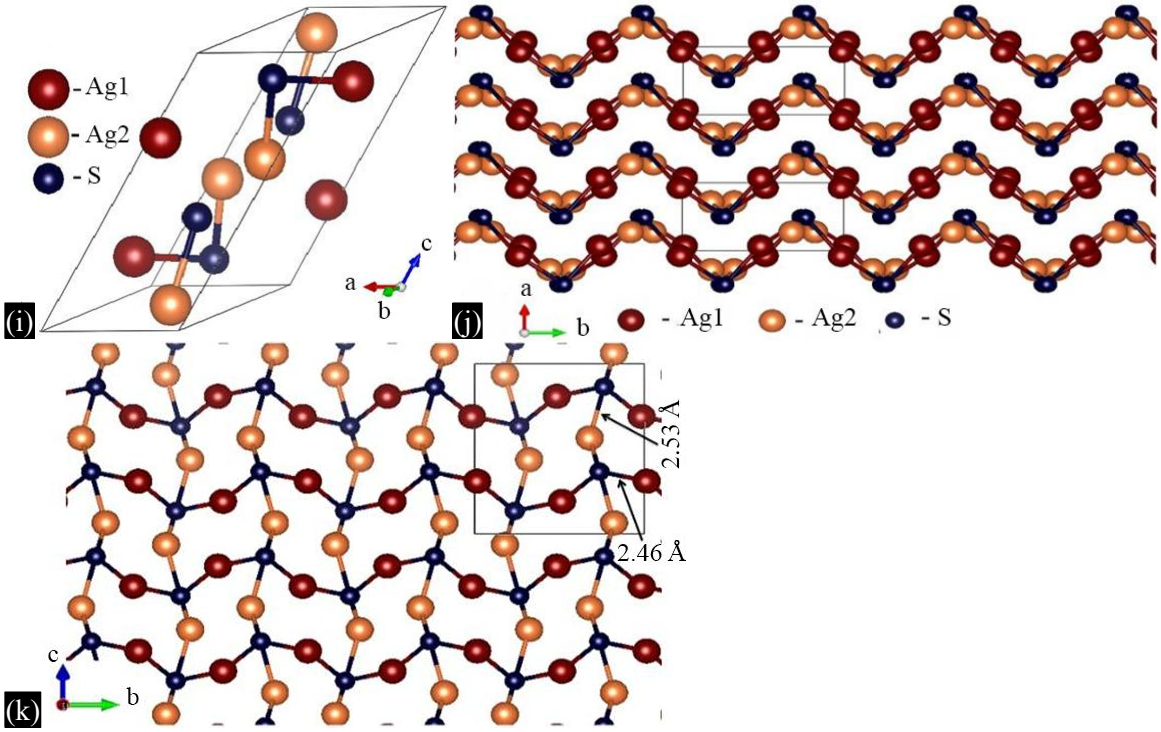

Figure 2. (Ag2S)1-xAgx powder XRD Rietveld refinement (a)–(h), with x = 0–21.1% indicated in square brackets and the amount of thiourea in each graph. The α-Ag2S crystal structures in (i) three-dimensional unit cells, (j) a-b planes, and (k) b-c planes. The Ag2S unit cell is shown as a rectangular box with grey lines in Figure 2(a)–(k).

Figure 2(a)–(k) shows a typical atom configuration in monoclinic crystal structures (P21/c) of α-Ag2S. These structures are created using a CIF file that was acquired following Rietveld refinement of ASA0's XRD using VESTA software. Ag atoms occupy two distinct 4e Wyckoff sites, namely Ag1 (0.0715, 0.0151, 0.3093) and Ag2 (0.7264, 0.324, 0.4375), while sulphur atoms occupy one 4e site, S (0.492, 0.2339, 0.1321). This is the unit cell of α-Ag2S, as shown in Figure 2(i). Figure 2(j) shows clear slipping planes (100) layered along the <100> direction. For α-Ag2S, zigzag atomic layers of (100) planes can slip along the <001> direction. A deformed 4 × Ag-S octagon makes up the Ag-S framework (Figure 2(k)). According to Figure 2(k), the Ag1−S bond length along the <010> direction is 2.46676 Å, while the Ag2−S bond length along the <001> direction is 2.53358 Å. The development of densely packed stoichiometric Ag2S nanocrystals is confirmed by the fact that their lengths are less than those of non-stoichiometric silver sulphide Ag1.93S [24-27].

Interestingly, the systematic synthesis of Ag2S-Ag composites at 160 oC requires careful cleaning procedures and appropriate stirring of the solution throughout the precursor process. Furthermore, ASA0, ASA1, ASA3, and ASA5 pellets are subjected to energy dispersive analysis of X-ray (EDX) measurements for compositional analysis. Table 1 lists the atomic percentage of the constituent elements in composites. Here, the elemental ratio of Ag:S is precisely 2:1, as indicated by ASA0. The presence of excess metallic Ag as a second phase is revealed in the instance of ASA1, however, when the Ag component is larger than the nominal value. This is created because sulphur is volatile, as shown by XRD data (Figure 1). The sulphur content in ASA3 and ASA5 is also lower than anticipated (Table 1).

Field Emission Scanning Electron Microscopy

Field emission scanning electron microscopy (FESEM) measurements are used to determine the size and shape of NPs for single phase Ag2S (ASA0) and heterostructure Ag2S-Ag (ASA6). This is done by spreading a fraction of the as-synthesised powder on a conducting carbon tape, which is then

Table 2. The nominal values of face-centered cubic (FCC) and monoclinic (M) Ag2S phases, as well as the elemental compositions of Ag2S-Ag nanocomposites, were acquired from EDX.

Elements	ASA0	ASA1	ASA3	ASA5
Observed Ag (atm. %) [nominal M+FCC]	61.5 (61.7)	67.6 (61.7)	69.7 (62.9+5.7 = 68.6)	70.4 (61.3+8.1=69.4)
Observed S (atm. %) [nominal M]	33.5 (33.3)	32.4 (33.3)	30.3 (31.4)	29.4 (30.6)

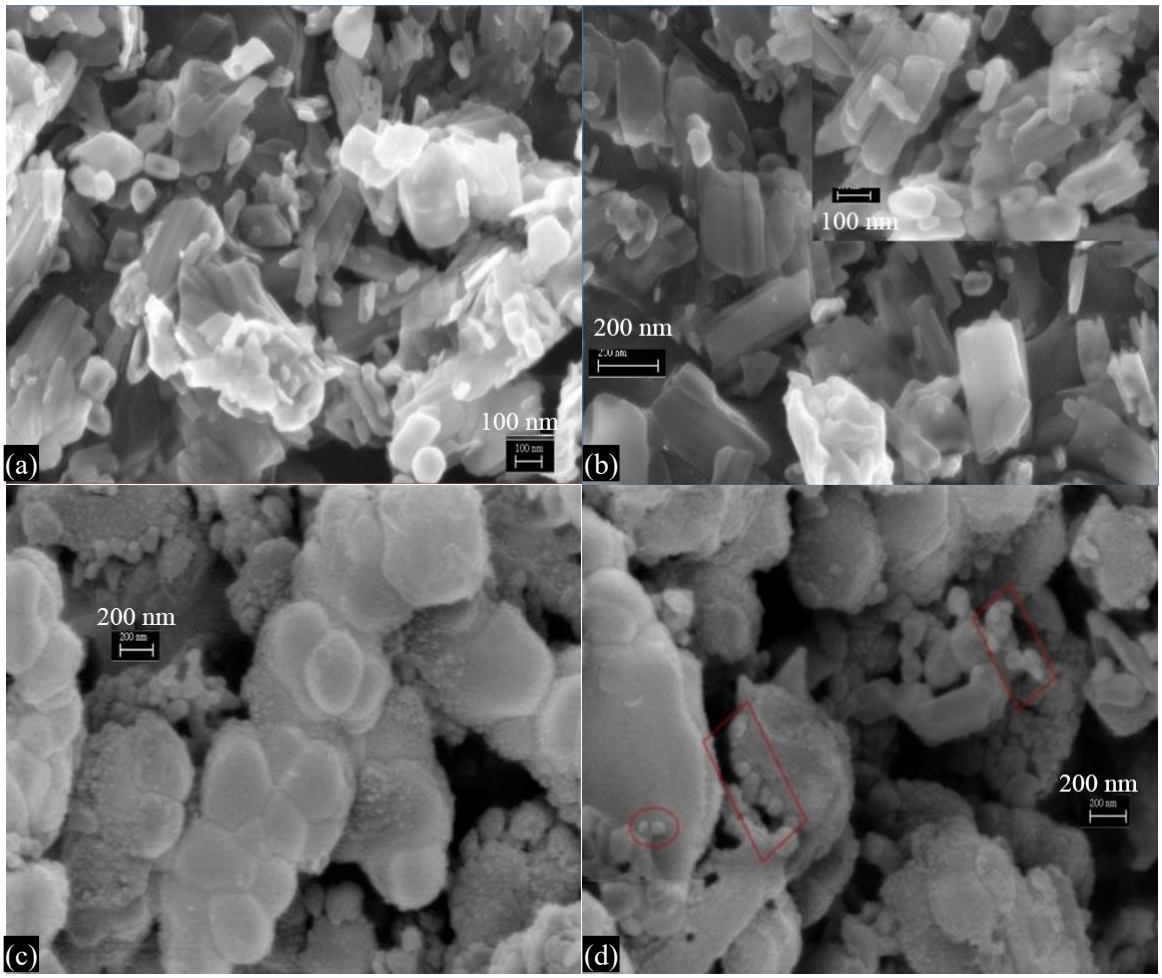

Figure 3. FESEM images of ((a) and (b)) Ag2S NPs (ASA0) and ((c) and (d)) Ag2S-Ag NCs (ASA6) at different magnifications.

coated with 10 gold (Figure 3(a)–(d)). These pictures demonstrate how particles come in a variety of shapes and sizes. The majority of the particles are observed in disc forms (circular, cubic, rectangular, or strip-like) with an average thickness of 52 nm and a wide range of lengths and widths between 50 nm and several hundred nm (Figure 3(a) and (b)). However, the FESEM pictures of ASA6 reveal some extra spherical NPs connected to slightly thicker and clearer nanodisks (NDs). These spherical NPs, which range in diameter from 50 to 100 nm, may be Ag-NPs created as a result of the reaction's excess AgNO3 (Figure 3(c) and (d)). Additionally, some larger particles are seen, which could be the result of smaller NPs aggregating (Figure 3(a)–(d)).

We collected location-specific EDX of ASA6 by concentrating the electron beam on individual ND of Ag2S (Figure 4(a)) and spherical NPs of Ag (Figure 4(b)) to highlight the production of Ag2S and Ag heterostructures in ASA6 nanocomposites. The atomic ratio of Ag:S was nearly exactly 2:1 when

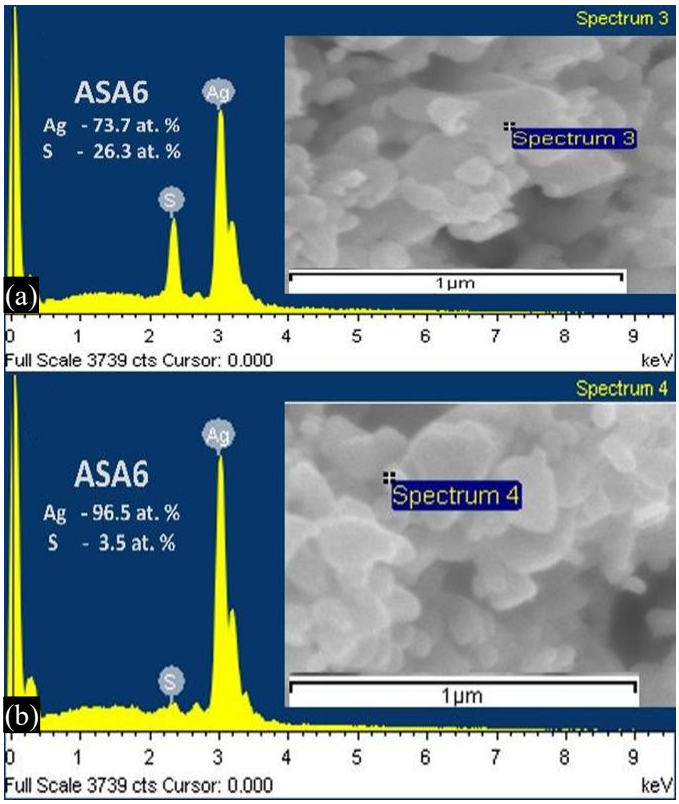

Figure 4. Electron beam size was focused at extremely small sections of (a) a larger nanodisk and (b) a smaller spherical nanoparticle to get the Ag2S-Ag nanocomposite (ASA6) EDX spectra. Spots of interest are denoted by "::" (four points), and insets show FESEM pictures of matching samples.

EDX was performed on crushed pellets of ASA0 (Ag2S) (Table 2). However, when examining disk-shaped Ag2S (Figure 4(a)), the ratio is 73.7:21.3, which is significantly higher than 2:1 and indicates the presence of excess Ag on Ag2S nanodisks ((Figure 3(c) and (d)). In order to verify this, EDX data were gathered from three distinct spherical NPs. The average atomic ratio of Ag:S is 91.5:3.5, which amply demonstrates that these spherical NPs may be the most Ag NPs. Because the spot size and penetration depth of the electron beam utilised are bigger than the size of the targeted particles, the presence of around 3.5 at.% sulphur is expected to arise from larger Ag2S NPs underneath Ag NPs. Furthermore, an electron beam has the ability to enter the Ag2S ND. This supports our hypothesis that the bigger disk-shaped particles are Ag2S coated or bonded to smaller spherical Ag NPs and/or excess Ag atoms, possibly in an amorphous form [28-37].

Ag-content increases in composites when extra Ag atoms begin nucleating and forming smaller Ag metal nanoparticles on the surface of larger Ag2S nanodisks, according to these FESEM pictures and EDX analysis of Ag2S-Ag nanocomposites (ASA0 and ASA6). Additionally, as the composites' Ag content rises, the size of the Ag NPs grows as well. At the same time, some of the larger Ag NPs separate from the Ag2S disc surface. Consequently, the presence of two types of NPs (Ag2S and Ag) combined in the composite is demonstrated by FESEM in conjunction with EDX analysis of ASA6. These findings are well supported by the previously mentioned Rietveld XRD improvements.

Zeta Potential Study

In NanoPlus 3, 2 mg of synthesised NPs are dispersed in deionised (DI) water at 25 oC in order to determine the zeta potential (ζ) of ASA0 and ASA6. ASA0 and ASA6 have average ζ potentials of -25.4 mV and -11.2 mV, respectively (Figure 5(a)). Ag2S-Ag nanocomposites are unstable in DI water at 25 oC, as indicated by their ζ values, which are smaller than ±30 mV [6,37]. The lower ζ value for

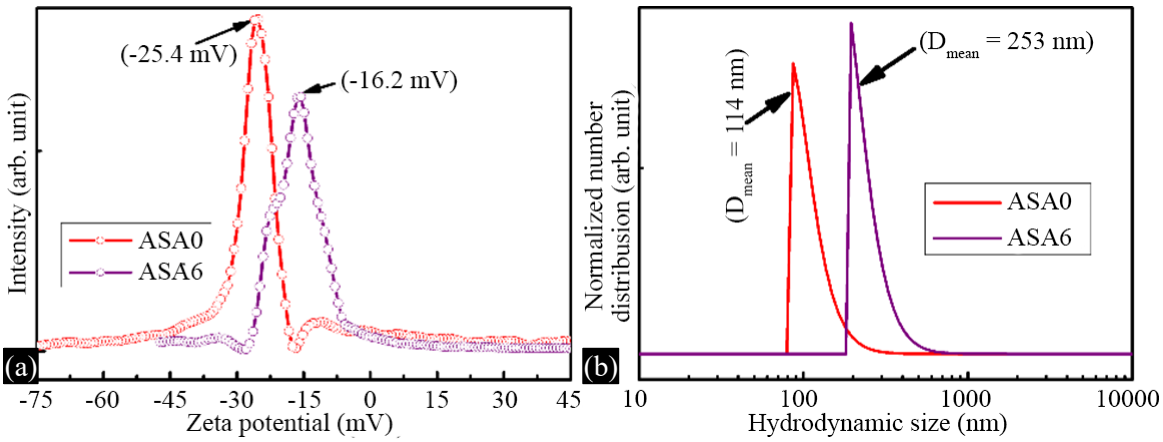

Figure 5. (a) Zeta potential and (b) hydrodynamic diameter spectra of ASA0 and ASA6 NPs dispersed in deionised water.

ASA6 compared to ASA0 indicates that Ag NPs are joined to Ag2S NPs, increasing their hydrodynamic size and, thus, decreasing their mobility (Figure 5(b)). Since the mobility of NPs in solution under the applied electric field (E = 85 V/cm) is directly proportional to the value, the addition of Ag nanoinclusions to Ag2S NPs alters its surface charge [6,37]. With a strong correlation to ζ values, the mean hydrodynamic diameters (Dmean) for the identical solution of ASA0 and ASA6 as in the related ζ measurements are 114 nm and 253 nm, respectively. This finding would imply that Ag NPs are linked to Ag2S NPs, increasing the Dmean values.

X-ray Photoelectron Spectroscopy

With the ability to probe down to a few nm, X-ray photoelectron spectroscopy (XPS) is used to further examine surface information on Ag_2S-Ag nanocomposites. The lack of impurity elements is confirmed by the survey scan spectrum of ASA1, which was synthesised using the nominally needed quantity of initial precursors and recorded in the region of 0 to 1300 eV (Figure 6(a)). For a thorough investigation of their valence states, the high resolution spectra of C, Ag, S, and O are recorded (Figure 6(b)–(e)). The carbon 1s peak can be deconvoluted into three peaks, which are designated as the C 1s peaks for C-C/C=C, -C-OH, and -C=O [6], respectively. These peaks are centred at 284.6 eV, 281.5 eV, and 288.12 eV (Figure 6(b)).

For whole spectra, the C 1s peak (284.6 eV) is used as the internal reference. The Ag 3d spectrum is deconvoluted into two peak pairs in Figure 6(c). The binding energies of Ag 3d5/2 and Ag 3d3/2 of the Ag+ ions in Ag2S should be attributed to the first pair of peaks, which appear at 367.51 eV and 373.5 eV, respectively [29–32]. Ag 3d5/2 and Ag 3d3/2 of metal Ag0 may be responsible for the smaller components at 368.25 eV and 374.21 eV on the higher energy side [29–32]. The presence of a fraction of Ag0 atoms in the composite was validated by the relative spectrum intensities between Ag0 and Ag+ components (Figure 6(c)). Two peaks that can be attributed to S 2p3/2 [31] and S 2p1/2 [29,30] are obtained by deconvolution of the S 2p peak, and they are situated at around 160.8 eV and 162.02 eV, respectively (Figure 6(d)).

UV-visible Absorption And Photoluminescence Spectroscopy

To validate further the existence of Ag2S and Ag together in the heterostructured nanocomposites, we performed UV-vis absorption spectroscopy for samples synthesized with varying the quantities of thiourea (Figure 7(a)–(c)). Ag2S NPs (ASA0) dispersed in de-ionized water show two obvious absorption edges, first at 260 nm due to the n → σ* transition of non-bonding electrons of sulphur in Ag2S with Ag- S bonds [19,33]. This result also confirms the absence of unreacted AgNO3 in the products for which absorption peak is expected at 300 nm [34]. Second, its blue-shifted optical band gap [13,15,16] is responsible for the absorption peak edge at around 600 (600-700) nm, which is in line with the mode found for Ag2S NPs [13,15,16,19]. However, as the Ag content increased in all

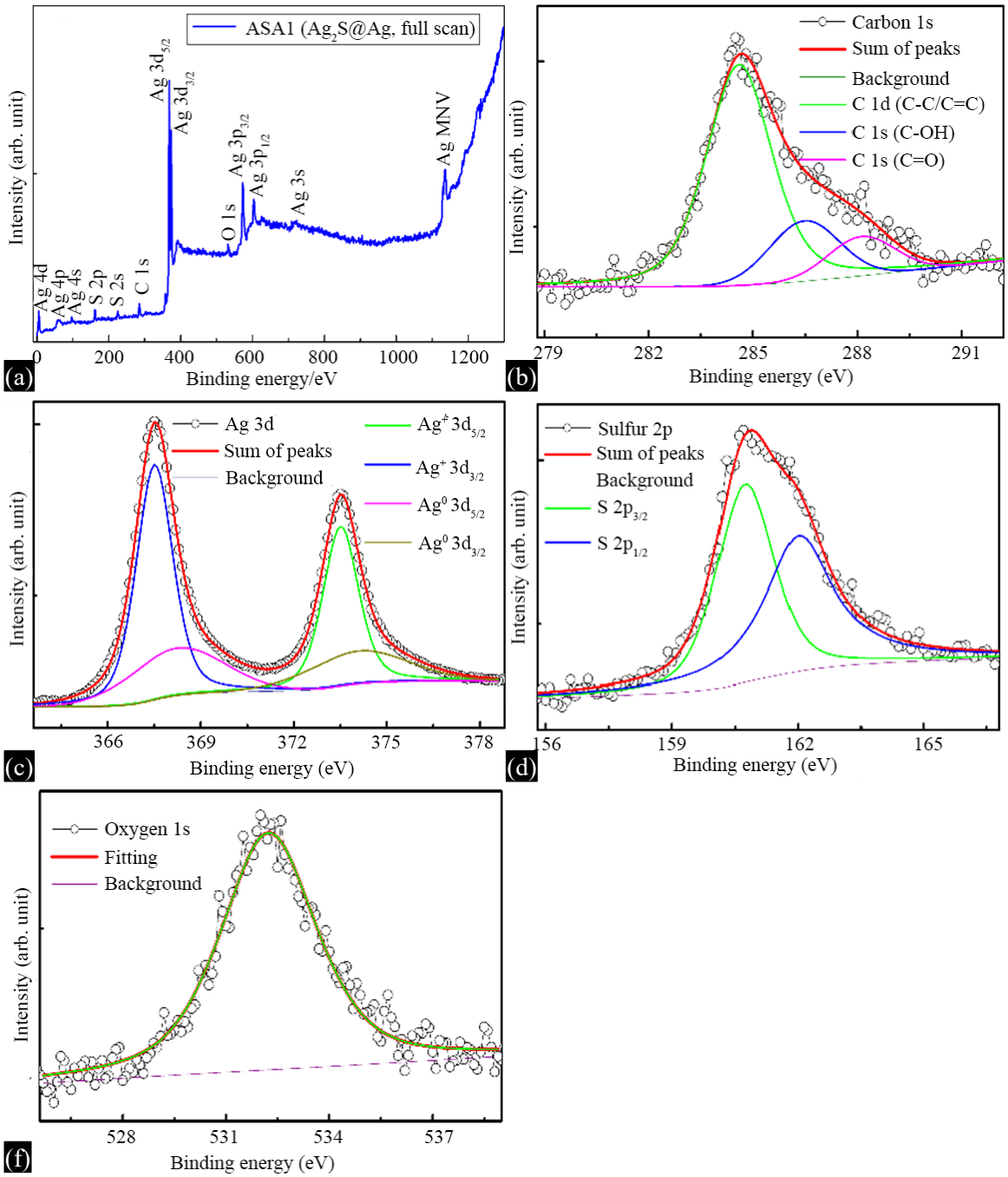

Figure 6. (a) Full survey scan XPS spectrum of ASA1. High resolution XPS spectra of (b) Carbon 1s, (c) Ag 3d, (d) S 2p and (e) Oxygen 1s. Experimental data are represented by black open circle and red curve is fitting line which is the summation of all peaks.

other samples, the Ag2S nanoparticles' optical absorption edges moved towards the longer wavelength region. The absence of the expected additional broad absorption edge peaks in the visible region (320–500 nm) that would have resulted from the emergence of metallic Ag NP surface plasmon resonance (SPR) in Ag2S-Ag nanocomposites is explained by the NPs' high sensitivity to aspect ratio [35] and environmental influences [29,35,36]. This could provide more proof that Ag NPs adhere well to Ag2S nanodisks, supporting the findings of EDX.

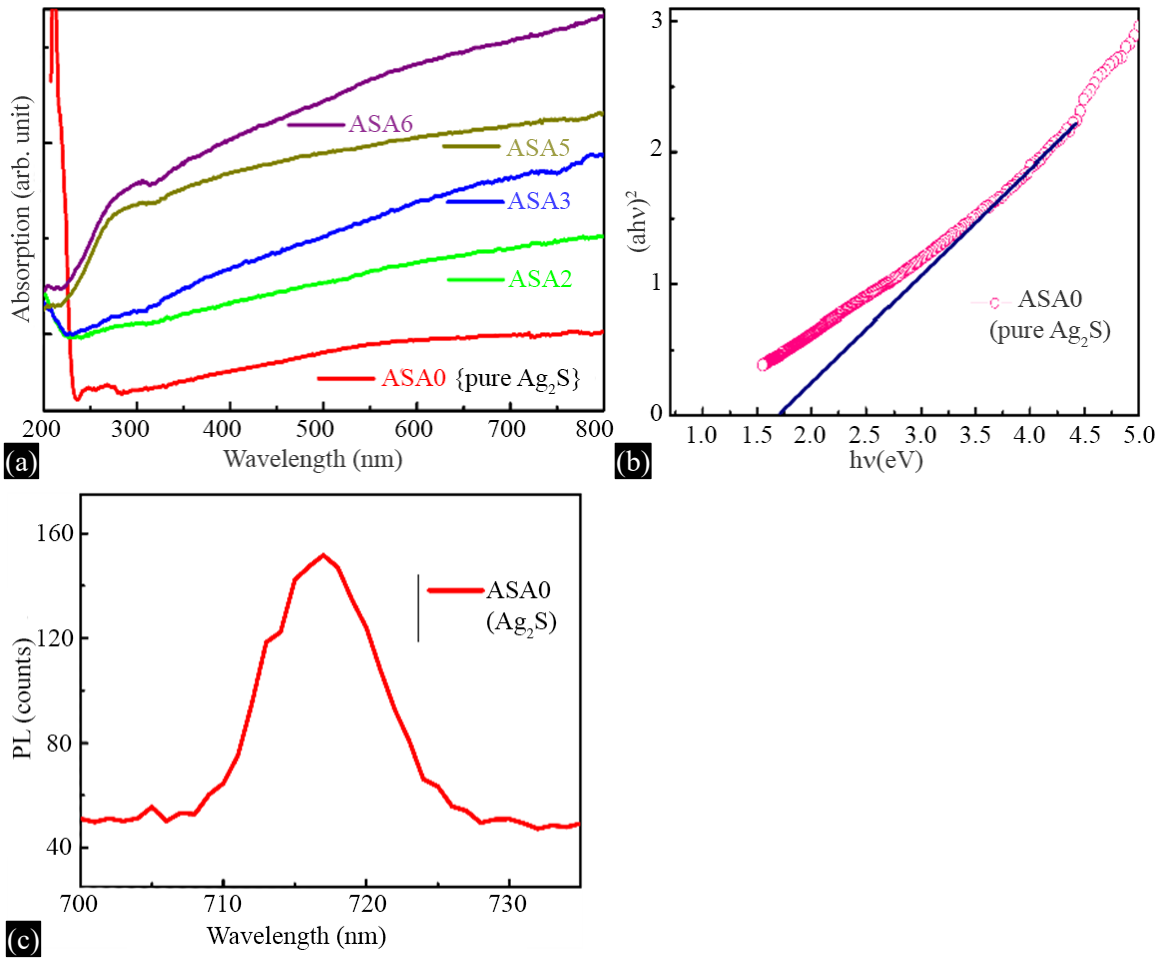

Figure 7. (a) UV-visible absorption spectra of Ag2S-Ag nanocomposites with Ag- nanoinclusions of 0 – 23.5 % in Ag2S host and (b) Tauc plots of ASA0. (c) Photoluminescence emission spectra of Ag2S (ASA0) collected using exciting wavelength of 476 nm.

In actuality, the bottom of the conduction band of Ag2S and the Fermi level of metallic Ag are situated at -4.42 eV and -4.26 eV, respectively, from the vacuum level (Figure 8(a)) [29]. The near-Fermi level conduction electrons of metallic Ag will occupy the empty, low energy states accessible in Ag2S when Ag NPs and Ag2S NPs come into contact, facilitating electron transfer (Figure 8(b) and (c)). This charge transfer from Ag NPs to Ag2S NDs is expected to cause the band-bending of the semiconducting side at the interface (Figure 8(b)) since a broad SPR mode that should be present at 320-500 nm is absent (Figure 7(a)). Additionally, this results in the development of a contact potential barrier that stops additional charge transfer.

This could indicate that many Ag NPs are unable to fully separate from the host Ag2S NPs and that, for instance, only a portion of Ag NPs easily enter solution (water) when they are disseminated in water. This is supported by the zeta potential (ζ) analysis of these composites with very low ζ values in deionised water (Figure 5), which shows that absorption occurs from very small or amorphous NPs in the solution while the majority of the larger crystalline particles settle at the bottom of the cuvette. Furthermore, the Tauc or Bardeen equation [16] is used to determine the optical band gap of Ag2S NPs using UV-visible absorption data (Figure 7(b)). As Ag2S is a direct band gap semiconductor, the straight line fit to a plot between (ahν)2 versus hν gives Eg, where a is the absorption coefficient and hν is the photon energy. The obtained band gap for the pure Ag2S (ASA0) is 1.7 eV, in good agreement with previously reported values of NPs [15,16,19].

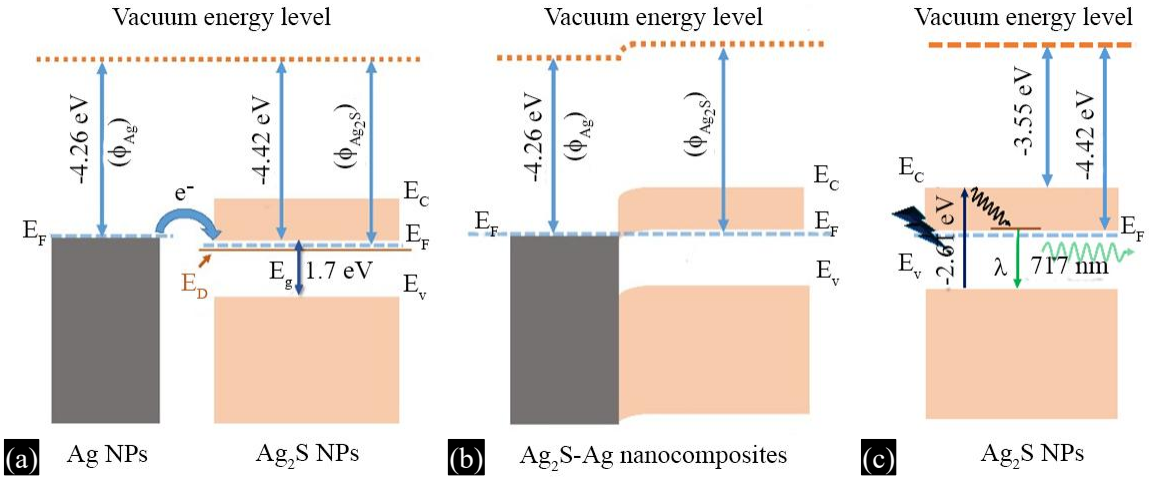

Figure 8. Schematics of (a) band diagram of separate Ag and Ag2S NPs, (b) band bending in Ag2S-Ag nanocomposites and (c) possible mechanism for observance of photo luminescence in Ag2S NPs.

To justify the above assumption, the photoluminescence (PL) emission spectra are collected for ASA0 (Ag2S) using laser exciting source of wavelength of 476 nm (2.6047 eV) (Figure 7(c)). The main emission peak of ASA0 (pure Ag2S) is centered at 717 nm (1.729 eV), which can be ascribed to the band gap recombination of electron–hole pairs [13,15,16,19]. The schematic of the PL phenomenon is illustrated in Figure 8(c).

Transport Properties

Prior to measuring the transport characteristics, any moisture or adsorbed EG on the powder samples were eliminated, as shown by the XPS results. To do this, pellets of every sample are created using a nominal pressure and placed in a tube furnace set at 200 °C for five hours while an Ar-gas flow of 160 cc/min is continuously applied. Following calcination, each pellet was ground into a fine powder, which was then compressed into pellets using pressure of around 1 GPa for one minute at 25 oC. Four-probe electrical resistivity (ρ) measurements are made in the pellets' bar-shaped portion, and thermopower (α) data is obtained for the final pellets.

Due to their high ρ, the ρ data for the ASA0 and ASA1 samples cannot be recorded using four-probe ρ measurements. Increasing the Ag-content on nanocomposites can reduce their high ρ [22]. The ρ data of Ag2S-Ag nanocomposites with different amounts of sulphur source are displayed in Figure 9(a)–(b). As contrast to ASA1, ASA2 (TU = 2.85 mmol) exhibits a strong decrease in ρ values, and its sharp exponential rise with decreasing temperature (Figure 9(a)) is explained by semiconducting behaviour. Furthermore, down to 225 K, the nanocomposite with 2.75 mmol TU (ASA3) exhibits semiconducting nature; below that, it displays metallic behaviour down to 5 K (Figure 9(b)). Other samples created with additional TU reduction show similar patterns, with the semiconducting to metal (SM) transition temperature (TSM) shifting towards the higher temperature side (Figure 9(b)–(d)). The final sample, ASA7 (2.55 mmol TU), shows a fully metallic nature throughout the 5-325 K range, and the SM transition vanished (Figure 9(b)).

Boundaries will go down linearly with decreasing temperature. These two competing phenomena operate together in these materials and domination of one over the other at different T regions are thus evident (Figure 9(a)–(b)). All samples (with Ag- nanoinclusions of 0-23.5%), except ASA7 showed semiconducting ρ below 325 K down to about 220 K maximally but with varying ranges because ρAg< ρAg2S here since electric current follows the least resistive path, thus below TSM all samples have to perhaps switch to metallic ρ. Below a particular temperature (TSM), ρAg will exhibit lower values as compared to ρAg2S, because ρAg goes down linearly and ρAg2S increase exponentially with decreasing T, and exhibits semiconductor to metal transition.

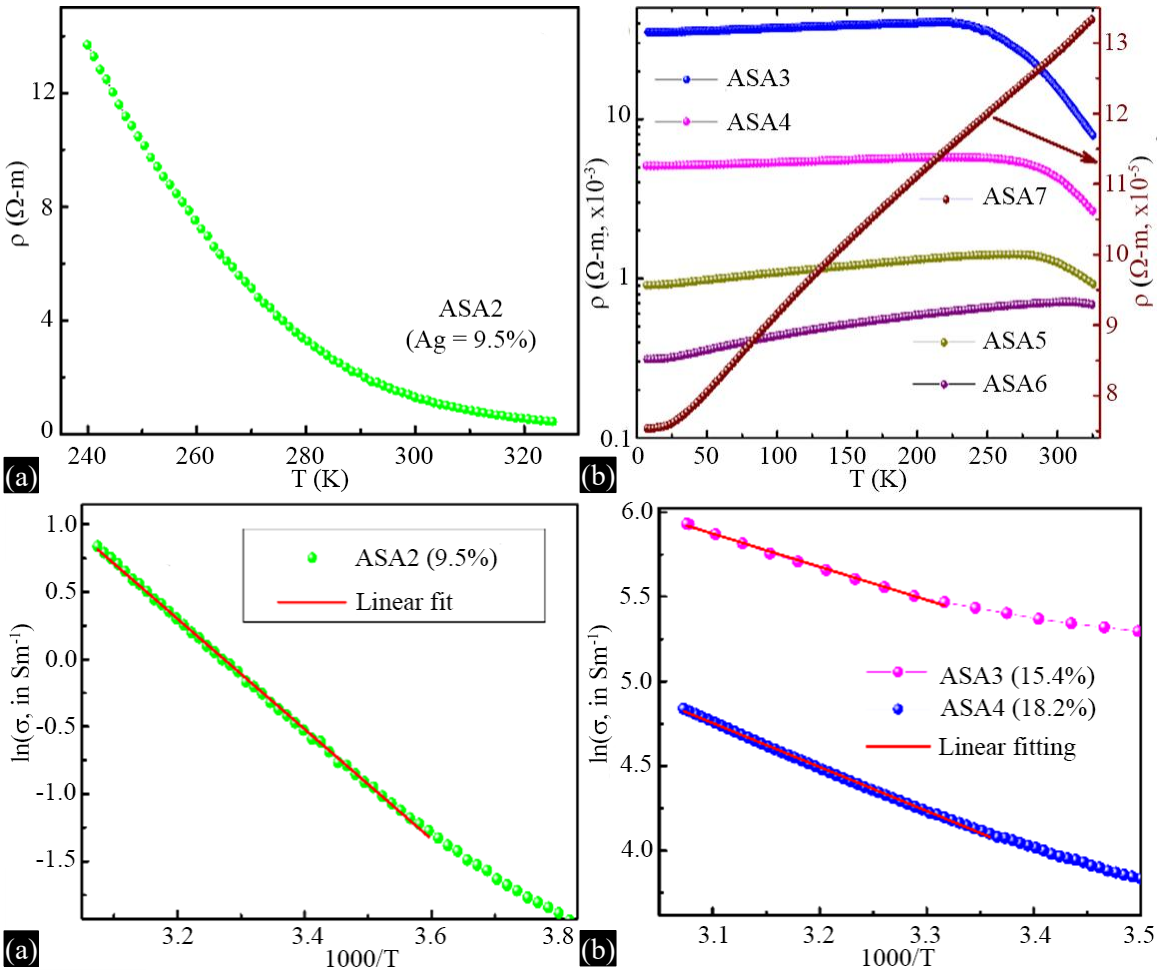

Figure 9. (a-b) Temperature dependent electrical resistivity of Ag2S-Ag nanocomposites with different % of Ag-nanoinclusions (9.5-23.5%) and (c-d) Arrhenius equation fitting of σ data near 300 K for ASA2, ASA3 and ASA4.

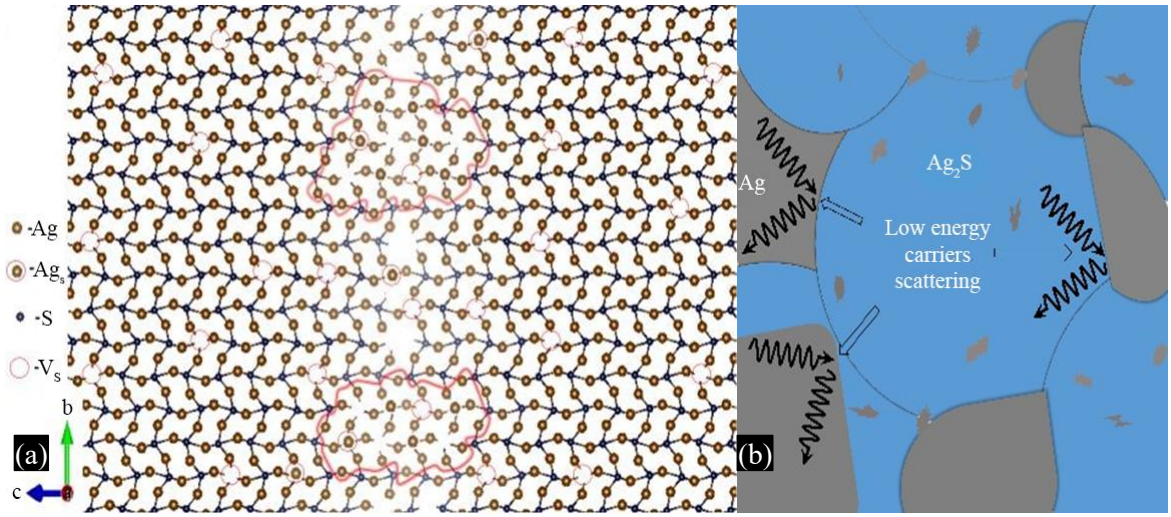

Figure 10. Diagram showing (a) the formation of Ag antisite defects (AgS) and sulphur vacancies (VS) in Ag2S, as well as the (b) potential scattering of low energy carriers at the semiconductor to metal interfaces in Ag2S-Ag nanocomposites, and the nucleation centers for Ag NPs at the Ag-rich grain boundary regions of two neighbouring grains (region inside the pink solid line). Ag atom clusters are indicated by very tiny grey patches in (b).

Table 3. The activation energy (Eac) and energy difference (Es) between bottom of conduction band (Ec) and Fermi level (EF) obtained from theoretical fitting of ρ and α data. Obtained α, α2σ and TE figure of merit at 325 K for Ag2S-Ag nanocomposites.

Sample name (Ag %)	Eac (meV)	ES= EC-EF (meV)	α (μV/K)	α2σ (μWm-1K-2)	ZT
ASA2 (9.5)	252.85	178.61	-581.3	0.77	0.15 x 10-3
ASA3 (15.4)	223.9	164.67	-229.8	1.50	1.03 x 10-3
ASA4 (18.2)	168.93	162.69	-162.1	9.92	
ASA5 (20.1)		158.42	-134.5	19.53	2.88 x 10-3
ASA6 (23.5)		55.57	-52.8	4.06	
ASA7 (21.1)			-0.3	0.0006	

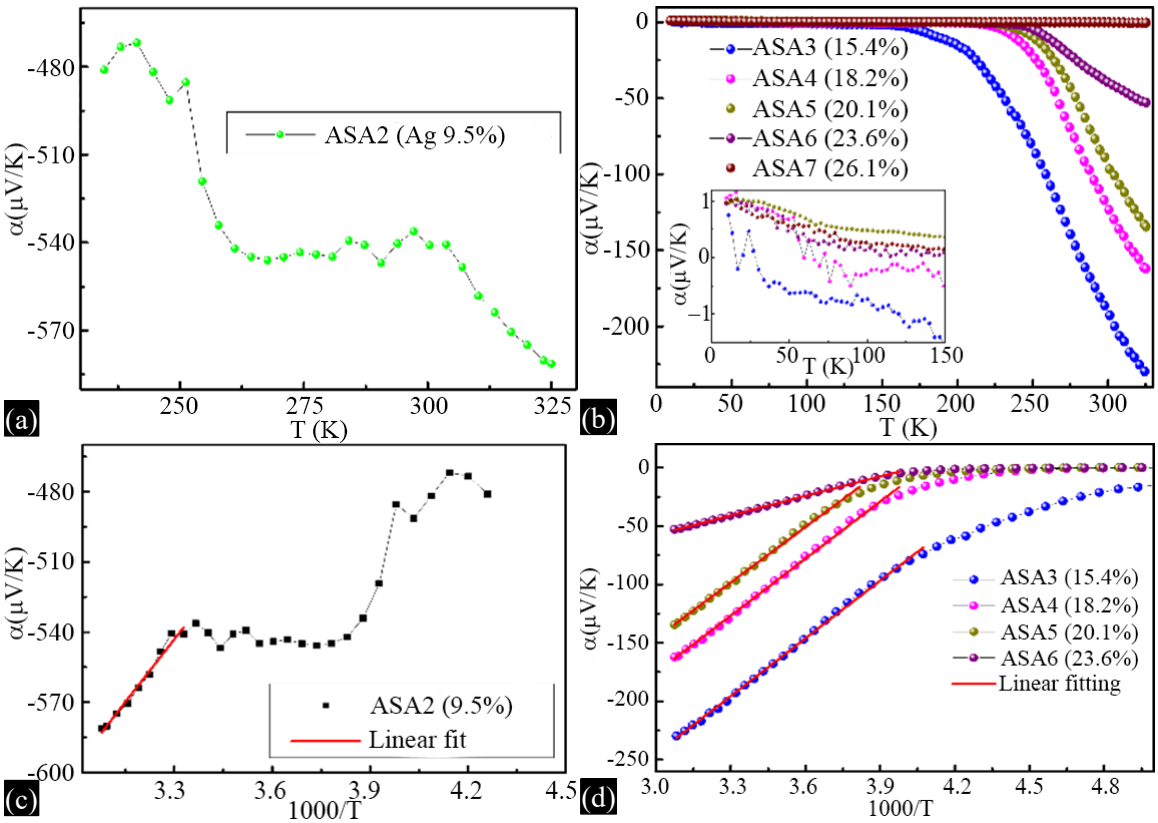

Figure 11. (a-b) Seebeck coefficient (α) and (c-d) linear fitting of α using Mott's equation for non-degenerate semiconductor of Ag2S-Ag nanocomposites synthesized with different ratios of initial precursors. Inset in (b): expanded portion of α in smaller scale.

Pure Ag2S (ASA0) and the first ASA1 nanocomposite are examples of highly resistive samples for which Seebeck coefficient (α) measurements are likewise not feasible (Table 3). As previously mentioned, the ρ of composites decreases as the Ag content increases because of the concurrent production of crystalline or amorphous Ag NPs at the grain boundaries and an increase in the number of sulphur defects in the Ag2S matrix (Figures 9(a)–(b) and 10(a)). As a result, total n rises with Ag in composites, enabling the use of a tiny temperature differential (~2 K) to generate detectable voltage. It is commonly known that the Seebeck coefficient α can reflect a relatively tiny change in n and that the inverse relation $\alpha \propto 1/n$ exists [1,6,37]. ASA2 (9.5% Ag NPs) is a more resistive sample with low n and shows very high α values (-574 μV/K at 325 K) with negative sign. Figure 11(a)–(b) shows the temperature dependence of α for ASA2 and all other samples with higher Ag-content, respectively. With decreasing T, the magnitude of α falls, and below 234 K, it exceeds the sensors' recordable range

(Figure 11(a)). These findings show that electrons make up the majority of charge carriers. It is determined that ASA2 is an n-type non-degenerate semiconductor based on its ρ analysis. Above their SM transition, the α values of other samples with higher Ag concentration (except from the most recent ASA7) likewise rise with T (Figure 11(a)–(d)).

As the amount of Ag in nanocomposites increases, the magnitude of α at 300 K progressively declines (αASA3> αASA4> αASA5> αASA6 at ~ 300 K). According to the $\alpha \propto 1/n$ connection, it is caused by a rise in carrier density (n) with Ag content [1,6,37]. The number of Ag NPs nucleation centers (amorphous clusters) in the grain boundary area rises with increasing Ag concentration, and the conjunction of these centers leads to the formation of fully developed Ag NP crystallites. Since conduction electrons are more likely to percolate through Ag grains and affective SM contacts are less common in composites with a higher Ag concentration, α values are suppressed to lesser values [11]. Because ASA2 has a low Ag concentration, Ag NPs are tiny and may disperse evenly. Because more SM contacts are created, the α values are large (α325K = - 575 μV/K). For ASA3, ASA4, ASA5, ASA6, and ASA7 nanocomposites, the α value at 325 K sequentially decreases to -229.7 μV/K, -162.2 μV/K, -134.5 μV/K, -52.8 μV/K, and -0.3 μV/K, respectively. These results show great agreement with both experiment [7,24,25] and theory [11,41]. They strongly imply that the insertion of metal NPs in semiconducting hosts, which causes the band bending at metal NPs to semiconductor interfaces, can lead to a large improvement in α (Figure 11(a)–(b)).

This exclusively transmits high energy carriers and can effectively block low energy charge carriers through an ideal potential barrier height at SM interfaces (Figure 10(b)). Since electrons are the primary charge carriers in both noble metal Ag and sulfur-deficient Ag2S [22,28], all nanocomposites should only show negative α values over the whole temperature range of 5–325 K. Although metallic Ag NPs in bulk have α values ranging from α5K = 0.5 to α 300K = 1.5 μV/K but with a negative Hall coefficient [38], below SM transitions, α values are suppressed to very small values for all samples and switch to positive values at low temperature. Its intricate Fermi surface with interconnected necks helps to explain this. The Fermi surface curvatures in FCC silver are positive, acute, and just touch the Brillouin zone boundary along each neck axis (111). The Fermi surface produces holes because the density of hole-like states, nh, connected to the <111> necks is significantly higher than that of electron-like states, ne, connected to the <100> belly [38]. Consequently, the density of thermally excited holes is significantly greater than the density of electrons, resulting in a positive α. When a system contains two different kinds of charge carriers, the total thermopower is equal to the sum of αe (-ve) and αh (+ve). Thus, the dominance of electrons or holes over one another at a specific temperature range determines the amount and sign of total α (Figure 11(a)–(d)).

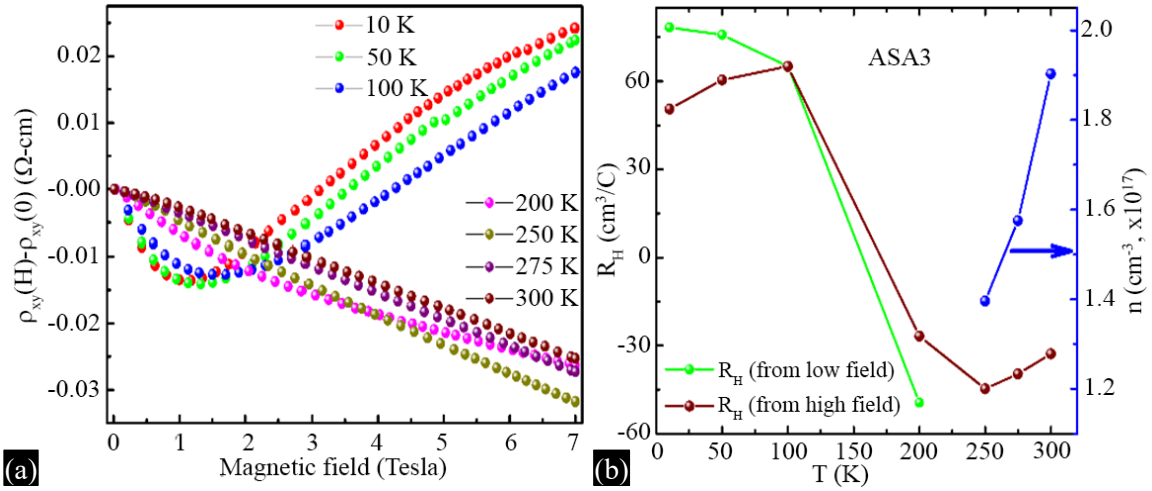

Figure 12. (a) Magnetic field dependent Hall resistivity ρxy and (b) calculated Hall coefficient (RH = slope of ρxy vs B curves) and charge concentration (n) of ASA3 at different temperature.

Different slopesfound from low and high Bz regions give different positive RH values below 200 K. These positive RH below 200 K is due to the complex Fermi surface in Ag2S-Ag nanocomposites and well consistent with α data in which very low or positive α values are attained (Figure 11(b)). The calculated density of defects states (NC) found (1.38x1020 cm-3) using n = NCexp(-(EC-EF)/kBT) is greater than n ~1.9x1017 cm-3 confirms the non-degenerate semiconducting nature of ASA3 at 300 K (Figure 12(a)–(b)).

CONCLUSIONS

We have demonstrated a facile method of synthesis of Ag2S-Ag nanocomposites and investigated the effect of Ag-nanoinclusions on their thermoelectric properties. The existence of Ag NPs as secondary phase in α-Ag2S is confirmed by Rietveld refinement of its powder XRD. A substantial reduction in electrical resistivity of Ag2S with decreasing sulphur content is observed and brings down to a measurable range. A significantly high Seebeck coefficient and power factor are achieved in 15.4 to 23.5 % Ag-nanoinclusions in semiconducting Ag2S. This Hall coefficient (RH) measurements are made for ASA3 and n values are computed in order to further establish the dominance of various charge carrier types at various T. The slope of the Hall resistivity (ρxy) vs applied magnetic field (Bz) graphs at various Ts would be known as RH. The slopes that are obtained at high temperatures (between 200 and 300 K) are negative, indicating that electrons represent the majority of charge carriers and thus the RH values are negative. The obtained n at 250-300 K is between 1-2 x1017 cm-3. Nevertheless, a change in the positive slopes with Bz is seen below 200 K, which indicates the presence of two different kinds of charge carriers with holes in the majority. opens up new strategy for enhancing the ZT value of this Ag2S near room temperature and beyond it. The next chapter details on trioctylphosphine-induced chalcogenide Bi2Te3- BiTe nanocomposites.

REFERENCES

1. A. Soni, Y. Shen, M. Yin, Y. Zhao, L. Yu, X. Hu, Z. Dong, K. A. Khor, M. S. Dresselhaus, and Q. Xiong, Nano Letter 12, 4305 (2012).
2. K. Biswas, J. He, I. D. Blum, C.-I Wu, T. P. Hogan, D. N. Seidman, V. P. Dravid and M. G. Kanatzidis, Nature 489, 414 (2012).
3. M. S. Dresselhaus, G. Chen, M. Y. Tang, R. Yang, H. Lee, D. Wang, Z. Ren, J.P. Fleurial and P. Gogna, Adv. Mater. 19, 1043 (2007).R. J. Mehta, Y. Zhang, C.
4. Karthik, B. Singh, R. W. Siegel, T. Borca-Tasciuc and G.Ramanath, Nature Mater. 11, 233 (2012).
5. M. Ibáñez, R. Zamani, S. Gorsse, J. Fan, S. Ortega, D. Cadavid, J. R. Morante, J. Arbiol, and A. Cabot, ACS Nano 7, 2573 (2013).
6. Tarachand, S. Hussain, N. P. Lalla, Y.-K. Kuo, A. Lakhani, V. G. Sathe, U. Deshpande and G. S. Okram, Phys. Chem. Chem. Phys. 20, 5926 (2018).
7. E. Lee, J. Ko, J.-Y. Kim, W.-S. Seo, S.-M. Choi, K. H. Lee, W. Shim and W. Lee, J.Mater. Chem. C 4, 1313 (2016).
8. S. Li, X. Liu, Y. Liu, F. Liu, J. Luo, F. Pan, Nano Energy 39, 297 (2017).
9. J. Androulakis, C.-H. Lin, H.-J. Kong, C. Uher, C.-I Wu, T. Hogan, B. A. Cook, T. Caillat, K. M. Paraskevopoulos and M. G. Kanatzidis, J. Am. Chem. Soc. 129, 9780 (2007).
10. Z. Peng, D. He, X. Mu, H. Zhou, C. Li, S. Ma, P. Ji, W. Hou, P. Wei, W. Zhu, X. Nie and W. Zhao, J. Electron. Mater. 47, 6 (2018).
11. S. V. Faleev and F. Léonard, Phys. Rev. B 77, 214304 (2008).
12. M. T. Barako, W. Park, A. M. Marconnet, M. Asheghi and K. E. Goodson, J. Electron. Mater. 42, 372 (2013).
13. X. Shi, H. Chen, F. Hao, R. Liu, T. Wang, P. Qiu, U. Burkhardt, Y. Grin and L. Chen, Nat. Mater. 17, 421 (2018).
14. R. S. Sharma and Y. A. Chang, Bull. Alloy Phase Diagrams 7, 263 (1986).
15. W. Jiang, Z. Wu, X. Yue, S. Yuan, H. Lu and B. Liang, RSC Adv. 5, 24064 (2015).
16. V. M. Huxter, T. Mirkovic, P. S. Nair and G. D. Scholes, Adv. Mater. 20, 2439 (2008).
17. B. Nowack, Science 330, 1054 (2010).

18. Z. Xu, Y. Bando, W. Wang, X. Bai and D. Golberg, ACS Nano 4, 2515 (2010).
19. X. Ma, Y. Zhao, X. Jiang, W. Liu, S. Liu, and Z. Tan, Chem. Phys. Chem. 13(10), 2531 (2012).
20. J. Xue, J. Liu, S. Mao, Y. Wang, W. Shen, W. Wang, L. Huang, H. Li, J. Tang, Mater. Res. Bull. 106, 113 (2018).
21. C. Xiao, J. Xu, K. Li, J. Feng, J. Yang and Y. Xie, J. Am. Chem. Soc. 134, 4287 (2012).
22. M. Adelifard and R. Torkamani, J Mater. Sci: Mater. Electron. 26, 7554 (2015).
23. A. M. Dehkordi, M. Zebarjadi, J. He, T. M. Tritt, Mater. Sci. Engineering R, 97, 1-22 (2015).
24. Q. Zhang, X. Ai, W. Wang, L. Wang, W. Jiang, Acta Mater. 73, 37 (2014).
25. M. Ibáñez, Z. Luo, A. Genç, L. Pivetau, S. Ortega, D. Cadavid, O. Dobrozhan, Y. Liu, M. Nachtegaal, M. Zebarjadi, J. Arbiol, M. V. Kovalenko, A. Cabot, Nat. Commun. 7, 10766 (2016).
26. S. Ortega, M. Ibáñez, Y. Liu, Y. Zhang, M. V. Kovalenko, D. Cadavid, A. Cabot,Chem. Soc. Rev. 46, 3510 (2017).
27. S. I. Sadovnikov, A. I. Gusev and A. A. Rempel, Phys. Chem. Chem. Phys., 17, 12466 (2015).
28. R. W. G. Wyckoff, Crystal Structures 1, 7 (1963).
29. M. Pang, J. Hu, and H. C. Zeng, J. Am. Chem. Soc. 132, 10771 (2010).
30. X. Wen, S. Wang, Y. Xie, X.-Y. Li, and S. Yang, J. Phys. Chem. B 109, 10100 (2005).
31. J. F. Moulder, W. F. Stickle, P. E. Sobol and K. D. Bomben, in Handbook of X-Ray Photoelectron Spectroscopy, ed. J. Chastain, Perkin Elmer Corp., Eden Prairie, MN, 1992.
32. J. R. Ansaria, N. Singh, S. Mohapatra, R. Ahmad, N. R. Saha, D. Chattopadhyay,M. Mukherjee, A. Datta, Appl. Surf. Sci. 463, 573 (2019).
33. X.-Y. Xie, L.-Y. Li, P.-S. Zheng, W.-J. Zheng, Y. Bai, T.-F. Cheng, J. Liu, Mater. Res. Bul. 47, 3665 (2012).
34. W. Su, S. S. Wei, S. Q. Hu and J. X. Tang, J. Hazard. Mater. 172, 716 (2009).
35. J. Xiong, C. Han, W. Li, Q. Sun, J. Chen, S. Chou, Z. Li and S. Dou, Cryst. Eng. Comm. 18, 930 (2016).
36. Tarachand, V. Sharma, R. Bhatt, V. Ganesan and G. S. Okram, Nano Research 9, 3291 (2016).
37. S. Fujita, A. Suzuki, Quantum theory of thermoelectric power (Seebeck coefficient). In: S. Kara (Ed.), Electromotive force and measurement in several systems. 2011. p. 1-20. In Tech.

